TU Delft

Delft University of Technology

# Radiofrequency safety of high permittivity pads in MRI—Impact of insulation material

Brink, Wyger M.; Remis, Rob F.; Webb, Andrew G.

**DOI**
10.1002/mrm.29580

**Publication date**
2023

**Document Version**
Final published version

**Published in**
Magnetic Resonance in Medicine

**Citation (APA)**
Brink, W. M., Remis, R. F., & Webb, A. G. (2023). Radiofrequency safety of high permittivity pads in MRI—Impact of insulation material. *Magnetic Resonance in Medicine*, *89*(5), 2109-2116. https://doi.org/10.1002/mrm.29580

**Important note**
To cite this publication, please use the final published version (if applicable).
Please check the document version above.

**Copyright**
Other than for strictly personal use, it is not permitted to download, forward or distribute the text or part of it, without the consent of the author(s) and/or copyright holder(s), unless the work is under an open content license such as Creative Commons.

**Takedown policy**
Please contact us and provide details if you believe this document breaches copyrights.
We will remove access to the work immediately and investigate your claim.

*This work is downloaded from Delft University of Technology.*
*For technical reasons the number of authors shown on this cover page is limited to a maximum of 10.*

Received: 26 September 2022 | Revised: 30 November 2022 | Accepted: 26 December 2022

DOI: 10.1002/mrm.29580

TECHNICAL NOTE

Magnetic Resonance in Medicine

# Radiofrequency safety of high permittivity pads in MRI—Impact of insulation material

**Wyger M. Brink**[1,2] | **Rob F. Remis**[3] | **Andrew G. Webb**[1]

[1]C.J. Gorter Center for High Field MRI, Department of Radiology, Leiden University Medical Center, Leiden, the Netherlands

[2]Magnetic Detection & Imaging Group, TechMed Centre, University of Twente, Enschede, the Netherlands

[3]Circuits and Systems Group, Department of Microelectronics, Delft University of Technology, Delft, the Netherlands

**Correspondence**
Wyger Brink, Magnetic Detection & Imaging Group, Technical Medical Centre, University of Twente, Hallenweg 5, 7522NH Enschede, the Netherlands.
Email: w.m.brink@utwente.nl

**Funding information**
H2020 European Research Council, Grant/Award Number: Advanced Grant NOMA-MRI

**Purpose:** High permittivity dielectric pads are known to be effective for tailoring the RF field and improving image quality in high field MRI. Despite a number of studies reporting benign specific absorption rate (SAR) effects, their "universal" safety remains an open concern. In this work, we evaluate the impact of the insulation material in between the pad and the body, using both RF simulations as well as phantom experiments.

**Methods:** A 3T configuration with high permittivity material was simulated and characterized experimentally in terms of $B_1^+$ fields and RF power absorption, both with and without electrical insulation in between the high permittivity material and the sample. Different insulation conditions were compared, and electromagnetic analyses on the induced current density were performed to elucidate the effect.

**Results:** Increases in RF heating of up to 49% were observed experimentally in a tissue-mimicking phantom after removing the material insulation. The $B_1^+$ magnitude and RF transceive phase were not affected. Simulations indicated that an insulation thickness of 0.5–2 mm should be accounted for in numerical models in order to ensure reliable results.

**Conclusion:** A reliable RF safety assessment of high permittivity dielectric pads requires accounting for the insulating properties of the plastic encasing. Ignoring the electrical insulation can lead to erroneous results with substantial increases in local SAR at the interface. Conversely, the material insulation does not need to be modeled to predict the $B_1^+$ effects during the design of the pad geometry.

**KEYWORDS**
dielectric pads, electromagnetic simulations, insulation, radiofrequency fields, safety

## 1 | INTRODUCTION

Performing MRI at higher static magnetic field strengths ($B_0$) has been an ongoing trend in MR technology, where the increased intrinsic SNR can be leveraged to increase spatial resolution or shorten acquisition time. Obtaining high quality MR images at higher fields can be challenging, however, in particular when the wavelength of the RF fields becomes similar or smaller than the dimensions of the body part that is being imaged. This is the case

This is an open access article under the terms of the Creative Commons Attribution License, which permits use, distribution and reproduction in any medium, provided the original work is properly cited.
© 2023 The Authors. *Magnetic Resonance in Medicine* published by Wiley Periodicals LLC on behalf of International Society for Magnetic Resonance in Medicine.



15222594, 0, Downloaded from https://onlinelibrary.wiley.com/doi/10.1002/mrm.29580 by Tu Delft, Wiley Online Library on [13/02/2023]. See the Terms and Conditions (https://onlinelibrary.wiley.com/terms-and-conditions) on Wiley Online Library for rules of use; OA articles are governed by the applicable Creative Commons License

for body imaging at $B_0 \geq 3$T where the RF wavelength is around 30 cm in muscle tissue, and neuroimaging at $B_0 \geq 7$T where the RF wavelength reduces to approximately 13 cm in brain tissue.[1] Under these conditions, a pronounced reduction in the uniformity of the RF magnetic transmit field ($B_1^+$) is observed, leading to undesirable spatial variations in image contrast.[2] Additionally, the increased levels of RF power deposition in tissue, for which safety limits are issued in terms of the specific absorption rate (SAR), can impose restrictive constraints on the sequence parameters, which can compromise the image quality gains when moving to higher fields.

Various RF technologies have emerged to address these challenges, both in the active form of parallel RF transmission using multiple independent RF transmitters, as well as in the form of passive materials such as high permittivity materials or "dielectric pads."[3] These flexible materials typically have a relative permittivity ($\varepsilon_r$) of approximately 100–500 and are positioned in between the volume RF coil and the human body. Various degrees of freedom in shaping the RF field can be addressed by modifying the material properties or the geometrical distribution using specialized software tools.[4] The passive approach offers a straightforward and practical solution, requiring no additional hardware or software changes nor pulse sequence modifications, and has therefore gained considerable attention from the MR community. Parallel RF transmission, on the other hand, introduces considerable additional hardware requirements as well as software overhead in terms of RF management, $B_1^+$ calibration sequences, and advanced SAR models.[5]

As with the development of customized RF transmit coils, the application of passive materials to manipulate the RF field warrants dedicated RF safety assessment, typically involving numerical simulations and validation experiments such as $B_1^+$ mapping and thermometry.[6] Despite the large body of literature reporting benign SAR effects of high permittivity materials,[7–21] their "universal" safety remains difficult to establish as their design may vary considerably. When the materials enhance the $B_1^+$ efficiency in the region of interest, reductions in SAR can be anticipated by virtue of the reduced RF power required by the system. Although the 10 g-averaged SAR ($SAR_{10g}$) distribution can be affected with local increases close to the material, the dominant peak $SAR_{10g}$ value is generally not increased even when considering similar RF input power levels.[10–12,16,18,19,21] Some reports have raised safety concerns, however, indicating potential increases in peak $SAR_{10g}$ of up to 160% depending not only on design parameters such as permittivity and pad geometry but also on RF field polarization, which are difficult to generalize.[22,23] At this point, it is not clear which conditions ensure safety compliance when using dielectric pads, nor have these effects been demonstrated or validated experimentally.

In light of these concerns, we hypothesized that the insulating materials in between the human body and the high permittivity material may explain at least some of the disparities in these findings, as this thin layer can be challenging to model in numerical simulation tools. In practice, such insulation would always be present, both in the form of the plastic container that is used to seal the materials, as well as in the form of the patient gown that is used during scanning. The most realistic approach would be to account for this insulating layer explicitly in the simulation model, however this requires a highly refined spatial discretization grid at the interface between the body model and the dielectric pad, which can be computationally demanding.[13,14,19] Some groups have recommended implementing a deliberate separation of 10 mm to reduce these computational demands, however such countermeasures can also reduce the $B_1^+$ enhancement and hamper the placement of pads in close-fitting receive arrays.[23] Further insights into the relevance of this insulation layer could also provide a handle into what numerical modeling strategy should be considered for obtaining a realistic RF safety assessment of high permittivity pads in MRI.

In this work, we aim to evaluate the effect of material insulation in the RF safety assessment of high permittivity materials employed in MRI. Electromagnetic (EM) simulations in a numerical body model are performed to evaluate the effect of material insulation on the $B_1^+$ field and SAR distribution. The observed effects are validated via $B_1^+$ mapping and MR thermometry in a rectangular phantom at 3T. The effects of different insulation conditions are then evaluated in a rectangular phantom through EM simulations. Finally, an EM analysis is performed on the induced current density to disentangle the role of conduction and displacement current densities on the observed results.

## 2 | METHODS

### 2.1 | Configuration

The study was guided by a 3T body imaging scenario where a single high permittivity pad was positioned at the anterior side of the male body model "Duke."[24] The effects of the high permittivity pad were evaluated when the material was either electrically insulated from, or in direct contact with, the human body (it should be noted that the latter configuration represents a "worst case scenario" in the sense both that the material would clearly never be placed in direct contact with the skin, and also that there is in practice always a scanning

15222594, 0, Downloaded from https://onlinelibrary.wiley.com/doi/10.1002/mrm.29580 by Tu Delft, Wiley Online Library on [13/02/2023]. See the Terms and Conditions (https://onlinelibrary.wiley.com/terms-and-conditions) on Wiley Online Library for rules of use; OA articles are governed by the applicable Creative Commons License

gown present on the patient). Further experimental and numerical studies were performed in an open rectangular phantom of size 32 × 24 × 11 cm, filled with an aqueous gel of polyvinylpyrrolidone (PVP-10) to establish dielectric properties similar to the human body ($\varepsilon_r$ = 48 and $\sigma$ = 0.50 S/m).[25] The material was gelled using 1% agarose to reduce thermal convection and allow for a dielectric pad to be positioned directly on top of the phantom material. A dielectric pad of size 18 × 18 × 1.5 cm was constructed using a 5:1 (weight ratio) suspension of $BaTiO_3$ powder in demineralized water, which resulted in dielectric properties of $\varepsilon_r$ = 307 and $\sigma$ = 0.16 S/m at 128 MHz.[8] The material was finally heat-sealed in polypropylene ($\varepsilon_r$ = 2.5, $\rho = 10^8\,\Omega$ cm) of approximately 500 μm thickness.

## 2.2 | EM simulations

Simulations of the transmit $B_1^+$ efficiency, RF transceive phase ($\phi^{\pm}$), dissipated power density ($P_d$), $SAR_{10g}$ distribution and induced current density ($\boldsymbol{J}$) were obtained in a high pass quadrature birdcage body coil model (61 cm diameter, 50 cm length) using the finite difference time domain method (XFdtd 7.4, Remcom inc., State College, PA). The simulation grid was set to a uniform spatial resolution of 2 mm within the RF coil and simulations were performed using graphics processing unit (GPU) acceleration (Tesla K40c, NVIDIA, Santa Clara, CA). The SAR averaging procedure was set to exclude the high permittivity pad, in order not to bias local SAR effects close to the dielectric material due to density weighting (i.e., assuming that the material is thermally isolated from the body). All simulation data were normalized to the RF input power, unless specified otherwise.

A rectangular phantom model was used to evaluate the effect of different insulation conditions by varying insulation thickness and electrical resistivity, as well as the effect of different pad permittivities. All model perturbations were performed around a baseline dielectric pad with a relative permittivity of $\varepsilon_r$ = 300, $\sigma$ = 0.16 S/m and with 500 μm of polypropylene insulation. The rectangular geometry of the phantom enabled refining the simulation grid down to 50 μm around the interface to ensure that an accurate representation of the insulation layer was obtained in all cases.

A more specific vector analysis on the induced current densities was performed in which the total electric current density ($\boldsymbol{J}_{tot}$) was decomposed into a conduction currents ($\boldsymbol{J}_c$) and displacement currents ($\boldsymbol{J}_d$), as follows:

$$\begin{aligned}\boldsymbol{J}_{tot} &= \boldsymbol{J}_c + \boldsymbol{J}_d \\ &= \sigma\boldsymbol{E} + j\omega\varepsilon_0\varepsilon_r\boldsymbol{E}\end{aligned} \quad (1)$$

where $\boldsymbol{E}$ denotes the electric field, $j$ is the imaginary unit, $\omega$ is the angular RF frequency, $\varepsilon_0$ is the permittivity of vacuum, and $\sigma$ and $\varepsilon_r$ represent the conductivity and relative permittivity of the medium, respectively. Conduction currents are associated to energy absorption and RF heating, whereas displacement currents are associated with energy storage and a local enhancement of the $B_1^+$ field, based on a zero-order approximation of their effect.[26]

## 2.3 | MR protocol

Phantom experiments were performed on a 3T MRI system (Ingenia, Philips Healthcare, Best, the Netherlands) using the integrated quadrature body coil for RF transmission and a 32-channel torso array coil for signal reception. The protocol involved $B_1^+$ magnitude and RF transceive phase mapping using the DREAM sequence[27] (4 × 4 $mm^2$ in-plane resolution, 8 mm slice thickness, FOV = 384 × 384 $mm^2$, TR/TE = 4.6/2.3 ms, STEAM/imaging tip angle = 60°/10°) and MR thermometry via the PRF method[28] using a 20 min dynamic series of 3D gradient echo acquisitions (4 $mm^3$ isotropic resolution, FOV = 384 × 384 × 384 $mm^3$, TR/TE = 15/10 ms, tip angle = 10°). A preparation module consisting of a 100 kHz off-resonant rectangular RF pulse was added to increase the average RF power of the sequence to 100 W without interfering with image acquisition. Four cylindrical mineral oil phantoms were added to the setup to perform bias field correction by fitting the phase bias to a third order spherical harmonics basis.[29] The experiments were first performed without and then with the dielectric pad positioned directly on top of the phantom material. The polypropylene insulation was then removed and the protocol repeated.

# 3 | RESULTS

## 3.1 | EM simulations

Figure 1 shows transverse cross-sections of the $B_1^+$ efficiency and coronal maximum intensity projections of the $SAR_{10g}$ simulated in the male body model without and with high permittivity pad, either with a 2-mm insulation layer or in direct electrical contact with the body model. The $SAR_{10g}$ data were normalized to an average $B_1^+$ of 1 μT in the transverse cross-section of the body model, here, which corresponds to the RF calibration routine performed on many clinical MR systems. Although the 2-mm insulation layer has only a minor effect on the $B_1^+$ distribution, a 40% increase in peak $SAR_{10g}$ was observed in the torso when the high permittivity material was put in direct

15222594, 0, Downloaded from https://onlinelibrary.wiley.com/doi/10.1002/mrm.29580 by Tu Delft, Wiley Online Library on [13/02/2023]. See the Terms and Conditions (https://onlinelibrary.wiley.com/terms-and-conditions) on Wiley Online Library for rules of use; OA articles are governed by the applicable Creative Commons License

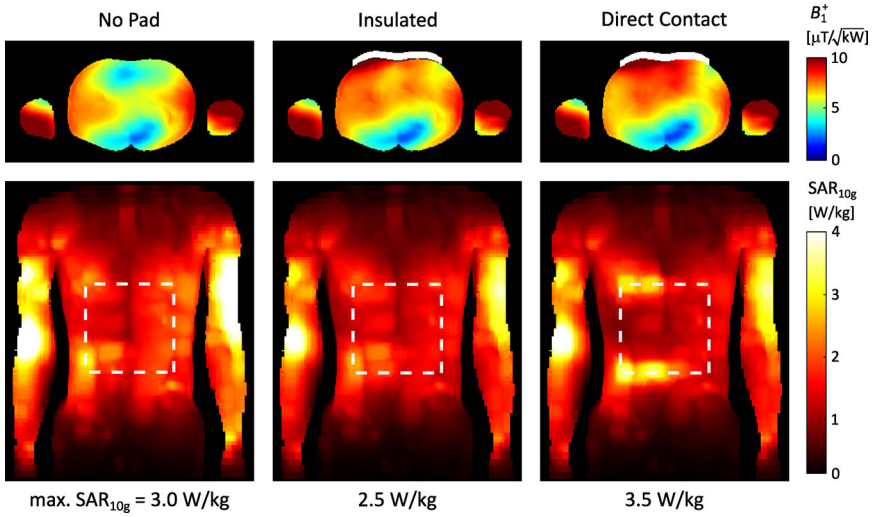


**FIGURE 1** Simulated effects of high permittivity material positioned on the anterior side of the male body model, with and without electrical insulation. Shown are transverse cross-sections of the $B_1^+$ efficiency (top) and coronal maximum intensity projections of $SAR_{10g}$ (bottom). SAR data were normalized to an average $B_1^+$ magnitude of 1 μT within the transverse cross-section of the body model. The position of the high permittivity material is illustrated in white.

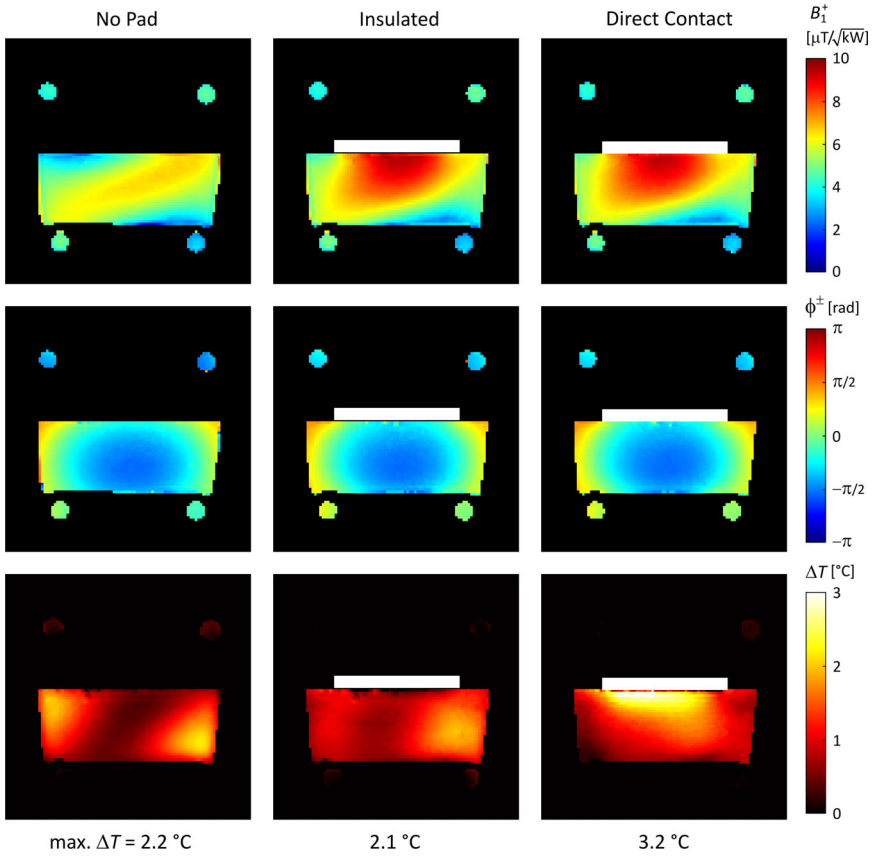


**FIGURE 2** Phantom measurements without and with the high permittivity pad in place, with and without electrical insulation. Shown are transverse cross-sections of the $B_1^+$ efficiency (top), RF transceive phase (middle), and temperature increases (bottom) after 20 min exposure at an average RF power of 100 W. The position of the high permittivity pad is illustrated in white, and the footers denote the maximum temperature increase.

electrical contact with the body, although the value is still well below the maximum value in the arms.

## 3.2 | Phantom experiments

Figure 2 shows the experimental RF characterization results with transverse cross-sections of the measured $B_1^+$ efficiency, RF transceive phase, and thermometry maps obtained in the rectangular phantom, both without and with the high permittivity pad positioned on top, first with the plastic encasing present and then in direct contact with the phantom material. The peak temperature increase with the insulated high permittivity pad was similar to that in the situation without pad, however this increased by 49% when the electrical insulation was removed and the high permittivity material was put in electrical contact with the phantom material. In both configurations with pad, the $B_1^+$ efficiency and RF transceive phase were minimally affected.

15222594, 0, Downloaded from https://onlinelibrary.wiley.com/doi/10.1002/mrm.29580 by Tu Delft, Wiley Online Library on [13/02/2023]. See the Terms and Conditions (https://onlinelibrary.wiley.com/terms-and-conditions) on Wiley Online Library for rules of use; OA articles are governed by the applicable Creative Commons License

### 3.3 | Phantom simulations

Simulations of the RF field in the rectangular phantom are shown in Figure 3, where the effects of insulation thickness, insulation resistivity and pad permittivity on the $B_1^+$ efficiency and $SAR_{10g}$ distribution were evaluated. The graphs show the peak $SAR_{10g}$ value in the phantom material close to the pad. The results indicated that an insulation thickness from 50 µm to 2 mm would result in a reduction of the peak $SAR_{10g}$, with an optimum thickness at around 500 µm, and that typical values for the electrical resistivity of polypropylene (>$10^8$ Ω cm) are more than sufficient not to influence $SAR_{10g}$. Finally, the pad permittivity is shown to also influence $SAR_{10g}$ with increases in peak $SAR_{10g}$ compared to baseline when the permittivity is excessively high (i.e., such configurations do not produce a useful $B_1^+$ distribution), which is in line with previous findings.[30]

Finally, Figure 4 shows sagittal vector plots of the induced current density and RF power absorption both with and without electrical insulation in between the high permittivity pad and the phantom. In both configurations, a strong displacement current density is evident within the dielectric pad, owing to its high permittivity. The configuration without electrical insulation featured a strong but very localized current density at the interface with the phantom, with both displacement ($\boldsymbol{J}_d$) as well as conduction ($\boldsymbol{J}_c$) components, which was not present in the situation with electrical insulation. This indicates that the direct electrical contact allows for a return path for the RF induced currents to be formed through the phantom, with a strong jump at the interface that is associated with local

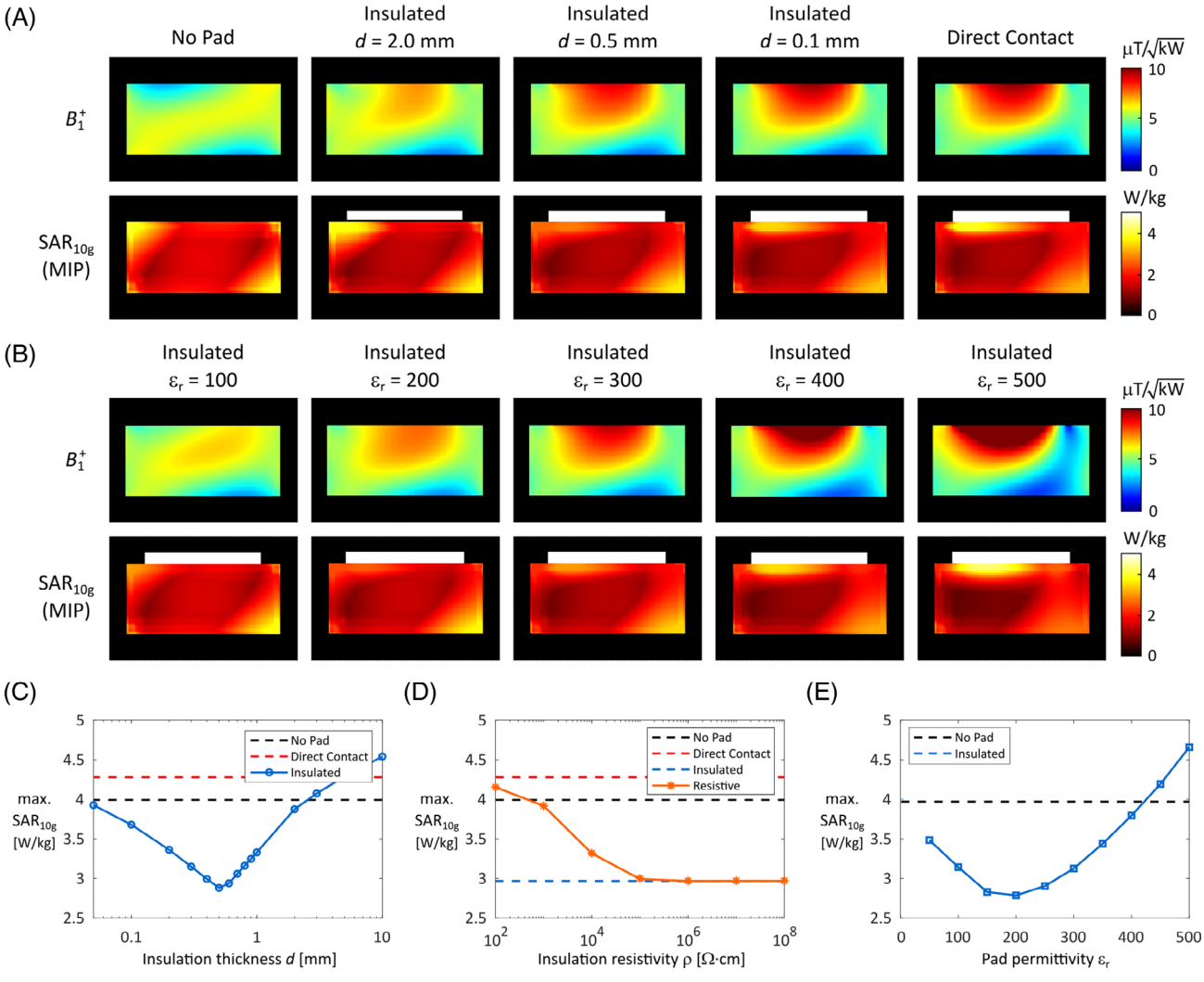


**FIGURE 3** Simulated $B_1^+$ and local SAR for different insulation conditions in the phantom configuration. The maps in (A) show transverse cross-sections of the $B_1^+$ efficiency and transverse maximum intensity projections of $SAR_{10g}$ for different insulation thicknesses. The maps in (B) show these for different pad permittivities. In (C–E), the variation in peak $SAR_{10g}$ as a function of the insulation thickness $d$, insulation resistivity $\rho$ and relative permittivity $\varepsilon_r$ of the pad is shown.

15222594, 0, Downloaded from https://onlinelibrary.wiley.com/doi/10.1002/mrm.29580 by Tu Delft, Wiley Online Library on [13/02/2023]. See the Terms and Conditions (https://onlinelibrary.wiley.com/terms-and-conditions) on Wiley Online Library for rules of use; OA articles are governed by the applicable Creative Commons License

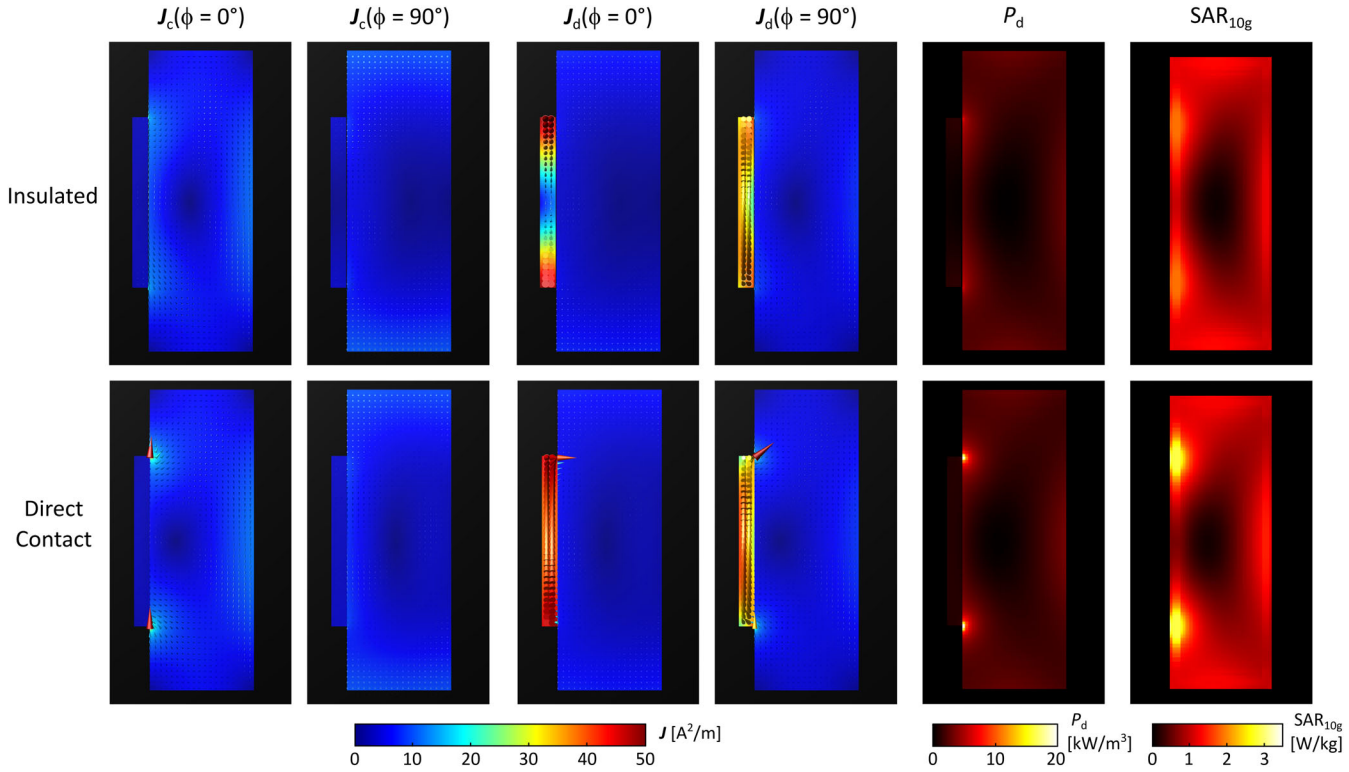


**FIGURE 4** Sagittal vector plots of the induced current densities in the simulated phantom configuration with (top) and without electrical insulation (bottom). Shown on the left are the conduction current density ($\boldsymbol{J}_c$) and displacement current density ($\boldsymbol{J}_d$), at two time-points within the oscillation. The right two columns show the dissipated power density ($P_d$) and $SAR_{10g}$. Without electrical insulation, both the conduction as well as the displacement current density show a strong local current density at the interface with the phantom, reflecting the formation of a return path or RF current "loop" with associated localized RF power absorption within the phantom material.

RF power absorption. An animated version is provided in Supporting Information Video S1.

## 4 | DISCUSSION AND CONCLUSION

This study demonstrates that a reliable RF safety assessment of high permittivity pads in MRI requires accounting for the insulating materials that are used in between the high permittivity material and the body. Increases in RF heating of up to 49% were observed in a tissue-mimicking phantom after removing the material insulation, confirming simulated effects. Simulations of the insulated configuration indicated that an insulation thickness of 0.5–2 mm is suitable for performing an RF safety assessment. Remarkably, the effect of material insulation on the $B_1^+$ field was minor, indicating that the material insulation does not need to be accounted for during the design of high permittivity pads.

The EM field analysis in this study showed that when the material insulation is removed, RF currents induced in the high permittivity material are able to form a current loop via the body. Due to the associated difference in permittivity, this leads to discontinuities in the normal component of the electric field, which is reflected in a strong localized current density that is induced at the interface as shown in Figure 4. This also results in a strong conduction current induced parallel to the interface, which is associated with localized RF power absorption and an increased local SAR.

Both the experimental data as well as simulations indicated that, while the RF heating pattern was considerably affected by the electrical insulation of the high permittivity material, both the magnitude of the $B_1^+$ field as well as the RF transceive phase were only minimally affected. This contrast may be attributed to the fact that the $B_1^+$ field is influenced mainly by the displacement current densities in the high permittivity material, while RF heating is dominated by the conduction currents induced in the sample. The strong and localized conduction current density at the sample interface leads to a very strong local increase in power absorption, while the corresponding localized displacement current density is insignificant compared to what is induced in the volume of the dielectric pad. This also indicates that methods to derive local SAR

15222594, 0, Downloaded from https://onlinelibrary.wiley.com/doi/10.1002/mrm.29580 by Tu Delft, Wiley Online Library on [13/02/2023]. See the Terms and Conditions (https://onlinelibrary.wiley.com/terms-and-conditions) on Wiley Online Library for rules of use; OA articles are governed by the applicable Creative Commons License

directly from measured complex $B_1^+$ field data may not be applicable to configurations that feature strong contrasts in permittivity.[31]

Additional simulations indicated that an insulating layer with a thickness of as little as 50 μm already reduce the RF currents that pass from the high permittivity material into the body. Common polymer thermoplastics provide more than adequate electrical insulation (i.e., $10^7$–$10^{14}$ Ω cm); however, some conductive counterparts can be found in the electronics industry and should be avoided.[32] Also, when a patient gown or clothing is present this would provide additional insulation, although the insulating properties can decrease due to humidity or moisture.[33] These results also indicate that configurations where high permittivity materials are in direct contact with body tissues, such as solid high permittivity ceramics that do not necessarily involve plastic encasings,[34] should be evaluated carefully before performing in vivo studies.

Accurate modeling of the thin insulation layer in numerical simulation tools can be a challenge, especially when the pad is positioned close to the curved interface of a voxelized body model. Some numerical simulation techniques such as the finite integration technique incorporate implicit material averaging,[35] which can affect the insulating properties of the pad interface. It can generally be recommended to use voxelized models of the high permittivity pads as this allows for the curvature of the pad to follow that of the body model, which improves electrical insulation. When computational resources allow, a discretization grid size of approximately 1–2 mm around the interface is recommended, with corresponding insulation thickness.

These results indicate that reliable RF safety assessments involving high permittivity materials for tailoring the RF field should be evaluated in an application-specific manner with adequate representation of the insulating materials present. The associated $B_1^+$ field effects show not to be as sensitive to these details, meaning that computational requirements may be relaxed during the design of the material distribution.

## ACKNOWLEDGMENT

European Research Council Advanced Grant NOMA-MRI.

## ORCID

*Wyger M. Brink* https://orcid.org/0000-0001-9974-7662
*Rob F. Remis* https://orcid.org/0000-0003-0365-4942
*Andrew G. Webb* https://orcid.org/0000-0003-4045-9732

## REFERENCES

1. Gabriel S, Lau RW, Gabriel C. The dielectric properties of biological tissues: III. Parametric models for the dielectric spectrum of tissues. *Phys Med Biol*. 1996;41:2271-2293.
2. Bernstein MA, Huston J, Ward HA. Imaging artifacts at 3.0T. *J Magn Reson Imaging*. 2006;24:735-746. doi:10.1002/JMRI.20698
3. Webb A. Dielectric materials in magnetic resonance. *Concepts Magn Reson A*. 2011;38:148-184. doi:10.1002/cmr.a.20219
4. van Gemert J, Brink W, Webb A, Remis R. High-permittivity pad design tool for 7T neuroimaging and 3T body imaging. *Magn Reson Med*. 2019;81:3370-3378. doi:10.1002/mrm.27629
5. Graesslin I, Vernickel P, Börnert P, et al. Comprehensive RF safety concept for parallel transmission MR. *Magn Reson Med*. 2015;74:589-598. doi:10.1002/mrm.25425
6. de Zanche N, van den Berg C, Brunner D, et al. *ISMRM Best Practices for Safety Testing of Experimental RF Hardware*. International Society for Magnetic Resonance in Medicine http://www.ismrm.org; 2022:1-119.
7. Teeuwisse WM, Brink WM, Webb AG. Quantitative assessment of the effects of high-permittivity pads in 7 Tesla MRI of the brain. *Magn Reson Med*. 2012;67:1285-1293. doi:10.1002/mrm.23108
8. Teeuwisse WM, Brink WM, Haines KN, Webb AG. Simulations of high permittivity materials for 7 T neuroimaging and evaluation of a new barium titanate-based dielectric. *Magn Reson Med*. 2012;67:912-918. doi:10.1002/mrm.24176
9. de Heer P, Brink WM, Kooij BJ, Webb AG. Increasing signal homogeneity and image quality in abdominal imaging at 3 T with very high permittivity materials. *Magn Reson Med*. 2012;68:1317-1324. doi:10.1002/mrm.24438
10. O'Brien KR, Magill AW, Delacoste J, et al. Dielectric pads and low- B1+ adiabatic pulses: Complementary techniques to optimize structural T1w whole-brain MP2RAGE scans at 7 tesla. *J Magn Reson Imaging*. 2014;40:804-812. doi:10.1002/jmri.24435
11. Brink WM, Webb AG. High permittivity pads reduce specific absorption rate, improve B1 homogeneity, and increase contrast-to-noise ratio for functional cardiac MRI at 3 T. *Magn Reson Med*. 2014;71:1632-1640. doi:10.1002/mrm.24778
12. Brink WM, van der Jagt MA, Versluis MJ, Verbist BM, Webb AG. High permittivity dielectric pads improve high spatial resolution magnetic resonance imaging of the inner ear at 7 T. *Invest Radiol*. 2014;49:271-277. doi:10.1097/RLI.0000000000000026
13. Brink WM, van den Brink JS, Webb AG. The effect of high-permittivity pads on specific absorption rate in radiofrequency-shimmed dual-transmit cardiovascular magnetic resonance at 3T. *J Cardiovasc Magn Reson*. 2015;17:82. doi:10.1186/s12968-015-0188-z
14. Luo M, Hu C, Zhuang Y, Chen W, Liu F, Xin SX. Numerical assessment of the reduction of specific absorption rate by adding high dielectric materials for fetus MRI at 3 T. *Biomed Tech (Berl)*. 2016;61:455-461. doi:10.1515/BMT-2015-0171
15. Yu Z, Xin X, Collins CM. Potential for high-permittivity materials to reduce local SAR at a pacemaker lead tip during MRI of the head with a body transmit coil at 3 T. *Magn Reson Med*. 2017;78:383-386. doi:10.1002/mrm.26344
16. Koolstra K, Börnert P, Brink W, Webb A. Improved image quality and reduced power deposition in the spine at 3 T using extremely high permittivity materials. *Magn Reson Med*. 2017;79:1192-1199. doi:10.1002/mrm.26721
17. Vaidya M v, Lazar M, Deniz CM, et al. Improved detection of fMRI activation in the cerebellum at 7T with dielectric pads extending the imaging region of a commercial head coil. *J Magn Reson Imaging*. 2018;48:431-440. doi:10.1002/jmri.25936

15222594, 0, Downloaded from https://onlinelibrary.wiley.com/doi/10.1002/mrm.29580 by Tu Delft, Wiley Online Library on [13/02/2023]. See the Terms and Conditions (https://onlinelibrary.wiley.com/terms-and-conditions) on Wiley Online Library for rules of use; OA articles are governed by the applicable Creative Commons License

18. Brink WM, Versluis MJ, Peeters JM, Börnert P, Webb AG. Passive radiofrequency shimming in the thighs at 3 Tesla using high permittivity materials and body coil receive uniformity correction. *Magn Reson Med*. 2016;76:1951-1956. doi:10.1002/MRM.26070
19. van Gemert J, Brink W, Remis R, Webb A. A simulation study on the effect of optimized high permittivity materials on fetal imaging at 3T. *Magn Reson Med*. 2019;82:1822-1831. doi:10.1002/MRM.27849
20. Yang QX, Wang J, Wang J, Collins CM, Wang C, Smith MB. Reducing SAR and enhancing cerebral signal-to-noise ratio with high permittivity padding at 3 T. *Magn Reson Med*. 2011;65:358-362. doi:10.1002/mrm.22695
21. Winkler SA, Rutt BK. Practical methods for improving B1+ homogeneity in 3 tesla breast imaging. *J Magn Reson Imaging*. 2015;41:992-999. doi:10.1002/JMRI.24635
22. Bitz AK, Kraff O, Orzada S, Herrmann T, Mallow J, Bernarding J, Ladd ME. RF safety evaluation of different configurations of high-permittivity pads used to improve imaging of the cerebellum at 7 Tesla. Paper presented at: Proceedings of the 23rd Annual Meeting of ISMRM; 2014; Milan, Italy, p. 4892.
23. Fiedler TM, Ladd ME, Bitz AK. Local SAR elevations in the human head induced by high-permittivity pads at 7 Tesla. Paper presented at: Proceedings of the 24th Annual Meeting of ISMRM, Singapore; 2015. p. 3213.
24. Christ A, Kainz W, Hahn EG, et al. The virtual family—development of surface-based anatomical models of two adults and two children for dosimetric simulations. *Phys Med Biol*. 2010;55:N23-N38. doi:10.1088/0031-9155/55/2/N01
25. Ianniello C, de Zwart JA, Duan Q, et al. Synthesized tissue-equivalent dielectric phantoms using salt and polyvinylpyrrolidone solutions. *Magn Reson Med*. 2017;80:413-419. doi:10.1002/mrm.27005
26. Brink WM, Remis RF, Webb AG. A theoretical approach based on electromagnetic scattering for analysing dielectric shimming in high-field MRI. *Magn Reson Med*. 2016;75:2185-2194. doi:10.1002/mrm.25783
27. Nehrke K, Börnert P. DREAM—A novel approach for robust, ultrafast, multislice B1 mapping. *Magn Reson Med*. 2012;68:1517-1526. doi:10.1002/mrm.24158
28. de Poorter J, de Wagter C, de Deene Y, Thomsen C, Ståhlberg F, Achten E. Noninvasive MRI thermometry with the proton resonance frequency (PRF) method: In vivo results in human muscle. *Magn Reson Med*. 1995;33:74-81. doi:10.1002/mrm.1910330111
29. Brink WM, Wu Z, Webb AG. A simple head-sized phantom for realistic static and radiofrequency characterization at high fields. *Magn Reson Med*. 2018;80:1738-1745. doi:10.1002/mrm.27153
30. Sica CT, Rupprecht S, Hou RJ, et al. Toward whole-cortex enhancement with an ultrahigh dielectric constant helmet at 3T. *Magn Reson Med*. 2020;83:1123-1134. doi:10.1002/MRM.27962
31. Katscher U, Voigt T, Findeklee C, Vernickel P, Nehrke K, Dössel O. Determination of electric conductivity and local SAR via B1 mapping. *IEEE Trans Med Imaging*. 2009;28:1365-1374.
32. Gulrez SKH, Ali Mohsin ME, Shaikh H, et al. A review on electrically conductive polypropylene and polyethylene. *Polym Compos*. 2014;35:900-914. doi:10.1002/pc.22734
33. Murphy EJ, Walker AC. Electrical conduction in textiles. I: The dependence of the resistivity* of cotton, silk and wool on relative humidity and moisture content. *J. Phys. Chem.* 1928;32:1761-1786. doi:10.1021/J150294A001/ASSET/J150294A001.FP.PNG_V03
34. Zivkovic I, Teeuwisse W, Slobozhanyuk A, Nenasheva E, Webb A. High permittivity ceramics improve the transmit field and receive efficiency of a commercial extremity coil at 1.5 Tesla. *J Magn Reson*. 2019;299:59-65. doi:10.1016/J.JMR.2018.12.013
35. Weiland T. Finite integration method and discrete electromagnetism. *Comput Electromagn*. 2003;28:183-198. doi:10.1007/978-3-642-55745-3_12


## SUPPORTING INFORMATION

Additional supporting information may be found in the online version of the article at the publisher's website.

**Video S1.** Sagittal vector animations of the induced current densities in the simulated phantom configuration with (top) and without electrical insulation (bottom) in between the phantom and the high permittivity material. Shown are the total induced current density ($\boldsymbol{J}_{\mathrm{tot}}$) decomposed into the conduction current ($\boldsymbol{J}_{\mathrm{c}}$) and displacement current ($\boldsymbol{J}_{\mathrm{d}}$) densities, respectively. The induced current densities show a strong local current density at the phantom interface when the high permittivity material is in direct contact, reflecting the formation of a return path or RF current 'loop' with associated RF power absorption.

**How to cite this article:** Brink WM, Remis RF, Webb AG. Radiofrequency safety of high permittivity pads in MRI—Impact of insulation material. *Magn Reson Med*. 2023;1-8. doi: 10.1002/mrm.29580

15222594, 0, Downloaded from https://onlinelibrary.wiley.com/doi/10.1002/mrm.29580 by Tu Delft, Wiley Online Library on [13/02/2023]. See the Terms and Conditions (https://onlinelibrary.wiley.com/terms-and-conditions) on Wiley Online Library for rules of use; OA articles are governed by the applicable Creative Commons License